

First measurements of periodicities and anisotropies of cosmic ray flux observed with a water-Cherenkov detector at the Marambio Antarctic base

Noelia Ayelén Santos^{a,*}, Sergio Dasso^{a,b,c}, Adriana María Gulisano^{b,c,d}, Omar Areso^b, Matías Pereira^b, Hernán Asorey^e, Lucas Rubinstein^{b,f}, for the LAGO collaboration

^aUniversidad de Buenos Aires, Facultad de Ciencias Exactas y Naturales, Departamento de Ciencias de la Atmósfera y los Océanos, Intendente Güiraldes 2160, C1428EGA, Ciudad Autónoma de Buenos Aires, Argentina

^bCONICET, Universidad de Buenos Aires, Instituto de Astronomía y Física del Espacio, Intendente Güiraldes 2160, C1428EGA, Ciudad Autónoma de Buenos Aires, Argentina

^cUniversidad de Buenos Aires, Facultad de Ciencias Exactas y Naturales, Departamento de Física, Intendente Güiraldes 2160, C1428EGA, Ciudad Autónoma de Buenos Aires, Argentina

^dInstituto Antártico Argentino, Dirección Nacional del Antártico, 25 de mayo 1143, San Martín, Buenos Aires, Argentina

^eCONICET, Universidad Nacional de San Martín, Instituto de Tecnologías en Detección y Astropartículas, Centro Atómico Constituyentes, Av. Gral. Paz 1499, B1650, Villa Maipú, Buenos Aires, Argentina

^fUniversidad de Buenos Aires, Facultad de Ingeniería, Departamento de Electrónica, Laboratorio de Acústica y Electroacústica, Av. Paseo Colón 850, C1063, Ciudad Autónoma de Buenos Aires, Argentina

Abstract

A new water-Cherenkov radiation detector, located at the Argentine Marambio Antarctic Base (64.24S-56.62W), has been monitoring the variability of galactic cosmic ray (GCR) flux since 2019. One of the main aims is to provide experimental data necessary to study interplanetary transport of GCRs during transient events at different space/time scales. In this paper we present the detector and analyze observations made during one full year. After the analysis and correction of the GCR flux variability due to the atmospheric conditions (pressure and temperature), a study of the periodicities is performed in order to analyze modulations due to heliospheric phenomena. We can observe two periods: (a) 1 day, associated with the Earth's rotation combined with the spatial anisotropy of the GCR flux; and (b) ~ 30 days due to solar impact of stable solar structures combined with the rotation of the Sun. From a superposed epoch analysis, and considering the geomagnetic effects, the mean diurnal amplitude is $\sim 0.08\%$ and the maximum flux is observed in ~ 15 hr local time (LT) direction in the interplanetary space. In such a way, we determine the capability of Neurus to observe anisotropies and other interplanetary modulations on the GCR flux arriving at the Earth.

© 2023 All rights reserved.

Cosmic Ray Detector, Cosmic Ray Solar Modulation, Space Weather

1. Introduction

It is well-known that the propagation of low-energy ($E \leq 10$ GeV) galactic cosmic rays (GCRs) is strongly influenced by the interplanetary magnetic field (IMF). Therefore, continuous monitoring of the GCR flux anisotropies and variabilities at individual ground stations is relevant for Space Weather (SW) research as it may serve as a tool for remote sensing of the IMF (e.g. Kudela et al., 2000; Potgieter, 2013).

There are several ground-based detector networks sensitive to different secondary cosmic rays (SCRs) that are generated in the particle showers initiated by primary cosmic rays (PCRs)

entering the upper Earth's atmosphere. For example: Neutron Monitors (NMs), Global Muon Detector Network (GMDN), Space Environment Viewing and Analysis Network (SEVAN) and Latin America Giant Observatory (LAGO), among others (e.g. Simpson, 2000; Rockenbach et al., 2014; Sidelnik & Asorey, 2017; Chilingarian et al., 2018).

The solar-controlled modulation of the GCR flux observed at Earth is generally divided into different types according to the timescale of the variation: the 22-yr, the 11-yr, the 27-day, the diurnal variation (DV) and the Forbush-type (Grieder, 2001). In addition to the aforementioned variations, there are several long-term periodicities (Potgieter, 2013) as well as a recently observed anomalous anisotropy specifically in the polar region (e.g. Gil et al., 2018).

Regarding the mean DV, it is produced by a stationary spatial

*Corresponding author

Email address: nsantos@at.fcen.uba.ar (Noelia Ayelén Santos)

anisotropy of the GCR flux in the interplanetary medium, which is observed from ground-level stations as a 24-hr temporal periodicity in SCR counting due to the Earth’s rotation. Based on the co-rotation theory, which involves the equilibrium between the radial outward convection of GCRs by the solar wind and the inward diffusion along the IMF, the maximum flux is observed when looking backwards along the orbit of the Earth around the Sun, 18 hr local time (LT) direction (Parker, 1964; Forman & Gleeson, 1975). The mean DV’s amplitude observed by NMs is $\sim 0.5\%$ and the maximum is in the ~ 14 -18 hr LT direction. Studies of long-term variations in the DV’s amplitude and phase suggest that it is strongly dependent on the solar cycle stages and the solar magnetic field’s polarity (*e.g.* Sabbah, 2013; Tezari et al., 2016).

In addition to the solar modulation, the effects of the magnetosphere and the Earth’s atmosphere also have to be considered to make a proper interpretation of ground-level observations. Two key concepts, such as the geomagnetic rigidity cut-off and the asymptotic cone of particle acceptance, allow us to describe all magnetospheric effects of GCRs (Belov et al., 2021).

About the Earth’s atmosphere, the two main causes of flux modulations are the barometric and the temperature effects. Both affect the mass distribution and, consequently, the associated production, absorption and decay processes of SCRs. The barometric effect is observed as an anticorrelation between the SCR flux and the barometric pressure variation at the observation level. This can be explained as a result of the rising absorption in the atmosphere due to the increased mass above the detector (*e.g.* Paschalis et al., 2013).

The main consequence of the temperature influence is a seasonal variation of SCR flux with a maximum in winter and a minimum in summer, particularly in ground-based detectors observing particles belonging to the electromagnetic (EM) and muonic components of the particle showers (*e.g.*, Tilav et al., 2010; Mendonça et al., 2016). Such muons are generated mainly by charged pions and kaons’ decay. The altitude of the muon main production layer occurs at ≈ 100 -200 hPa (Dorman, 2004). During summer, when the increase of this pressure level height arises due to the atmosphere’s expansion, the muons’ path length from the generation level to the observation level gets larger. Then, the probability of muon decay before reaching the detector increases and the observed flux decreases. The opposite occurs during winter. This is called “the negative temperature effect” and it dominates in ground-based observations. There are different methods (empirical and theoretical) to correct SCR counting for atmospheric temperature effects, and most of them depend on observations of atmospheric variables at different altitudes (Mendonça et al., 2016).

In 2019, a new water-Cherenkov detector (WCD) called Neurus was installed at the Marambio Argentinian Base in the Antarctic Peninsula for SW studies as part of the LAGO collaboration. In this work, we empirically analyzed the pressure and temperature effects on the data recorded by Neurus. This is a

crucial task for the data processing because it is only after removing the atmospheric modulations that the observed data are able to provide information on variations due to heliospheric and geomagnetic changes. In Section 2, we describe the detector and the acquisition system. In Section 3, we show the data selection. In Section 4, we analyze the barometric and temperature effects using data from ERA5’s atmospheric reanalysis (Hersbach et al., 2020). In Section 5, we perform a spectral analysis of the corrected count rate and analyze the DV’s periodicity. Finally, in Section 6 we present the conclusions.

2. A water-Cherenkov Detector for SW Studies

2.1. SW Antarctic Laboratory at Marambio Base

A WCD called Neurus was installed at the SW Antarctic laboratory of LAMP (an acronym for Spanish Laboratorio Argentino de Meteorología del esPacio), which is an interinstitutional group from Buenos Aires, Argentina, mainly dedicated to SW research, instrumental development, R2O-O2R, and real-time monitoring of SW conditions (Lanabere et al., 2020; Lanabere et al., 2021). The scientific aims of the Antarctic SW laboratory can be found in Gulisano et al. (2021).

The laboratory was deployed during the Argentinian Antarctic campaign in the southern hemispheric summer of 2019-2020 at the Argentine Marambio Base, located at 64.24S-56.62W and 196 m above sea level. Besides the particle detector, the laboratory has a magnetometer prototype, a GPS receiver to make the time stamp of observations, a meteorological station, and a telemetry system which provides 5-minutes real-time monitoring to the servers of the group in Buenos Aires.

Neurus WCD is part of the LAGO network (lagoproject.net; Sidelnik, 2016; Dasso et al., 2016; Sidelnik & Asorey, 2017). LAGO is a spin-off of the Pierre Auger Observatory with the concept of developing Cherenkov detectors, consisting of decentralized nodes spanning over Latin America, a region of the world not covered by the majority of the ground-based detector networks. WCDs operating in counting mode are highly sensitive to Forbush Decreases (Pierre Auger Collaboration, 2011; Dasso et al., 2012). They are robust, low-cost and, last but not least, easy-to-maintain and eco-friendly.

The effective geomagnetic cut-off rigidity of Marambio is $P_c = 2.1$ GV (<https://tools.izmiran.ru/>) High-latitude stations are privileged places because they are sensitive to lower-energy GCRs and have a narrower asymptotic cone of acceptance compared with sites located at middle and low magnetic latitudes (*e.g.* Bieber & Evenson, 1995; Mishev & Usoskin, 2020). Thus, they are interesting locations to study GCR anisotropies originated during their transport in the solar wind. Neurus, which is in a middle magnetic latitude site, it is the highest-latitude site of the LAGO collaboration. Besides that, it will be useful in the light of the recent similar measurements in the same geographic area (Zanini et al., 2017; Blanco et al., 2022).

Preliminary results from the LAGO Space Weather simulation chain can be found in Asorey et al. (2018) and Sarmiento-Cano et al. (2019). The authors simulate the geomagnetic effects on PCRs by using the MAGNETOCOSMICS code, the development of the air showers in the atmosphere is implemented by using the CORSIKA code, and finally a GEANT4 model is used for the detector's response. In particular, preliminary simulations for Marambio can be seen in Sarmiento-Cano et al. (2022).

The count rate of background low energy particles detected by the WCDs of the Pierre Auger observatory ($P_c \sim 9.5$ GV) are generated by PCRs with a median energy of about 90 GeV (Pierre Auger Collaboration, 2015; Dasso et al., 2012). Taking into account that the effective magnetic rigidity cut-off for Marambio is smaller ($P_c \sim 2$ GV), then the typical primary energies observed by Neurus are expected to be a few tens of GeV.

2.2. Neurus WCD

The WCD is made up of three main elements: the cylindrical tank, the PMT and the data acquisition system (DAQ) (see Figure 1). The tank is made of stainless steel (diameter = 0.96 m, height = 1 m) and it is filled with purified water.

This type of device is based on the possibility of detecting Cherenkov radiation from a charged particle passing through a volume of water. Charged particles from the shower of SCRs must have a minimum value of energy E_{min} to radiate Cherenkov light in water. For instance, for electrons and positrons (e^\pm) and muons (μ^\pm), which are the dominant components of the air showers at ground-level, $E_{min}^e \simeq 0.8$ MeV and $E_{min}^\mu \simeq 160$ MeV (Asorey et al., 2018). Also, high-energy photons ($E_{min}^\gamma \simeq 0.4$ MeV) could be detected due to the pair production process. In recent works, it has been shown that, by doping the water, the WCD shows an enhanced detection of high-energy neutrons (Sidelnik et al., 2020.)

The signal generated by muons is very different from the signal generated by electromagnetic particles. The typical energy of muons is $E_\mu \sim 1$ GeV and in a wide range of energies the stopping power of muons in water is ~ 2 MeV cm^{-1} (Pierre Auger Collaboration, 1996). Therefore, the majority of muons are able to pass through the entire detector losing only a small fraction of the initial energy and, in that case, the signal produced depends only on the length that the muons traveled in water. In the case of electrons, for the typical energy $E_e \sim 20$ MeV, the stopping power in water is ~ 2 MeV cm^{-1} . Then, the water volume is sufficient to absorb the majority of the electromagnetic particles (Pierre Auger Collaboration, 1996; Asorey, 2012).

The Cherenkov radiation produced is reflected and diffused by an internal coating made of Tyvek®. In this way, after a few reflections, all correlations between the propagation direction of the Cherenkov photons and the direction from which the particle enters to the detector is lost. This light is partially collected and amplified by a photo-multiplier tube (PMT), and then the DAQ acquires and digitizes the signal.



Fig. 1. (a) Neurus tank developed at IAFE in Buenos Aires; (b) Same tank and the DAQ system installed at the SW Antarctic Laboratory in the Antarctic Peninsula.

Three DAQ systems were implemented: (1) an oscilloscope (Rigol DS1102E) in rate mode counts the pulses that exceed a peak threshold of 0.02 V, and then they are recorded by a communication system in a computer (Mode A), (2) a commercial board Red Pitaya STEMLab 125-14 (14 bits resolution, 125MSPS, dynamic range ± 1 V), operating as an oscilloscope, records the trace of five sample pulses per second, limited by the acquisition speed of Red Pitaya in this mode (Mode B), (3) another Red Pitaya but working as an FPGA programmed as the LAGO's DAQ system which records the trace of all pulses detected (Mode C) (Arnaldi et al., 2019).

Each voltage pulse has three main characteristics which result from the convolution of the photon production Cherenkov and the response of the tank-Tyvek-PMT-DAQ system: duration (the average duration is approximately 100 ns), peak, and area under the curve (or charge). We consider 12×10^7 voltage pulses acquired by using Mode B during April-December, 2019.

In Figure 2, the charge histogram is presented. This shape is the typical one observed from a WCD (*e.g.* Bertou, 2006) and it is also well reproduced by simulations (*e.g.* Sarmiento-Cano et al., 2019).

The first local maximum (at lower charge) is related to the chosen trigger threshold, and it is mainly originated by EM component of the showers. Values around the second local maximum are related to muons. Particularly, pulses associated with this maximum, called muon hump, are linked with the passage of vertical and central muons across the detector. Signals with charges significantly greater than the one of the muon hump are originated by the entry of multiple particles into the detector (*e.g.* Durán et al., 2016).

Since a muon in water deposits ~ 2 MeV cm^{-1} and considering that the water level in the tank is 1 m, it is possible to assign an energy value of ~ 200 MeV associated with pulses charge equal to the second maximum of the histogram. In Figure 2, the position of the maximum was estimated by performing a quadratic regression getting $Q_{VEM} \approx 7$ V \times ns. The main goal of this calibration is to obtain the value of the Vertical-Equivalent Muon (VEM) in electronics units in order to assess

the quality of the measurements and also to compare them with Monte Carlo simulations.

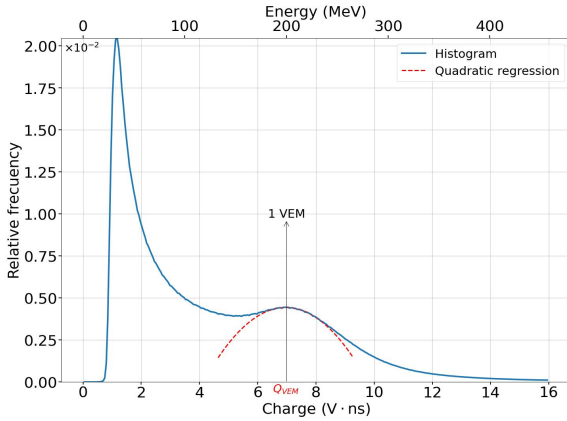


Fig. 2. Normalized charge histogram for the period April-December, 2019. The energy calibration was done by estimating the position of the second maximum (from the quadratic fit in dashed line), which is associated with the passage of vertical and central muons through the detector (~ 200 MeV).

3. Data Selection

In this work we use the hourly-average total count rate (S) measured by Neurus at Marambio, the hourly surface pressure measurement (P), and the room temperature (RT). S is built from the data acquired by the oscilloscope mode, which is the only DAQ system that has been working since the detector began its observations. We also use ERA5’s atmospheric reanalysis for the air column above Marambio.

In Figure 3, we show the observations from the installation (April 2019) to March 2021. We divided the whole period into three sub-periods to highlight and summarize the DAQ systems, the set-up of the observatory, and the improvements made in each one, namely:

(1): From April 1, 2019, to December 31, 2019. Two of the systems described in the previous section worked during this period: Mode A and B. There was no laboratory room temperature control.

(2): From January 1, 2020, to March 31, 2020 (2020 Antarctic campaign). The acquisition was stopped to carry out the updates.

(3): From April 1, 2020, to March 31, 2021. The Mode C and a laboratory room temperature control system were installed. The second update was carried out during the 2021 Antarctic campaign without stopping the acquisition. All the described modes (A, B and C) have been operational since then.

In this work, we analyze the data of the third period, in which the room temperature was stable to avoid different qualities of the measurements due to changes in the electronic devices’ behaviour. In this period, the mean values of these three variables are: 161.5 counts s^{-1} , 963 hPa and 25.6° C for S , P , and RT , respectively.

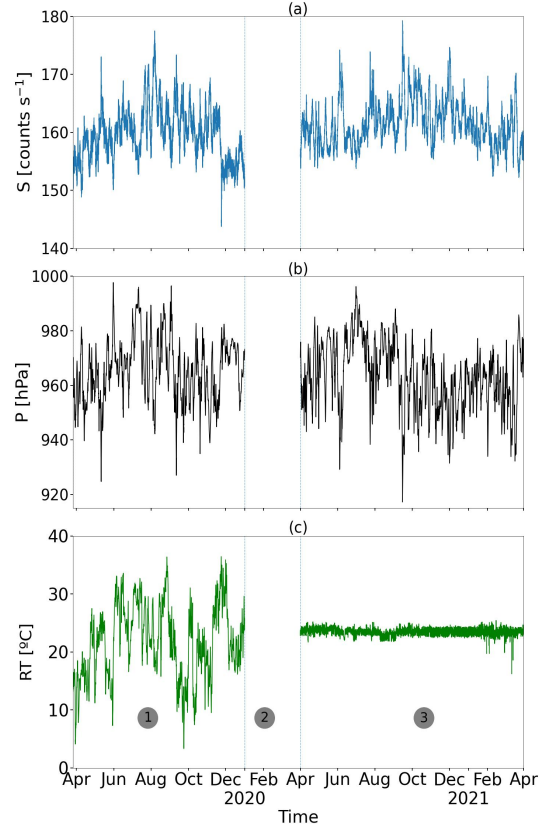


Fig. 3. Hourly-average raw total count rate S (a), surface pressure measurement P (b), and laboratory room temperature RT (c) from April 2019 to March 2021. The data are divided in three periods depending on the lab conditions. In this work data from the third period are used.

4. Analysis of the Atmospheric Effects on Counting Particles

4.1. Barometric Effect

The particle counting S of any SCR component varies with a small change in the atmospheric pressure P as $dS = \mu dP$, where μ is a negative coefficient that represents the absorption of the secondary component under consideration. By integrating this expression, supposing that for pressure P_0 the measured intensity is S_0 , and assuming $\mu = \text{const}$, an exponential dependence is obtained, as seen in Equation (1) (Grieder, 2001).

$$S(t) = S_0 e^{\mu(P(t)-P_0)} \quad (1)$$

Considering the first order approximation, Equation (1) could be expressed as:

$$\frac{\Delta S}{S_0} \times 100\% = \frac{S(t) - S_0}{S_0} \times 100\% \simeq \beta(P(t) - P_0) = \beta \Delta P \quad (2)$$

$\Delta S/S_0$ is the count rate relative variation and β is the barometric coefficient expressed in $\% \text{ hPa}^{-1}$.

We analyze the barometric effect during the time period April 2020-March 2021 splitting it into monthly intervals, P_0 , S_0 being the mean values of P , S for each month, respectively.

On Figure 4 there is an example of the observed data $\Delta S/S_0 \times 100\%$ vs. ΔP for July 2020. The expected negative correlation between both variables can be seen, with a relative variation of the counting up to 7% and a high Pearson correlation coefficient ($r = -0.9$). The red line is a linear fit based on Equation(2) and the slope $\hat{\beta}$ corresponds to the estimated barometric coefficient. Also, a linear fit was done (not shown here) considering Equation (1) and the relative difference between both $\hat{\beta}$ estimations is less than 1% in every month, then the linear approximation is good enough.

On Figure 5 we can see, for each month: (a) pressure variation ΔP range in which we observe that the greatest variations occur during winter (big atmosphere pressure variations during the crossing of meteorological fronts); (b) the Pearson correlation coefficient r between $\Delta S/S_0$ and ΔP ; (c) the slope $\hat{\beta}$ and its 95 % confidence interval. We estimated $\langle \hat{\beta} \rangle$ averaging monthly values and considering two standard deviation we get $\langle \hat{\beta} \rangle = (-0.19 \pm 0.02)\% \text{ hPa}^{-1}$. For this average, we considered months for which ΔP range is higher than 50 hPa. This way, these months had a considerable pressure variation and most of the variability was associated only with the barometric effect and not with other sources. The four selected months are indicated with a red X. We removed the pressure effect from the whole time period using this coefficient $\langle \hat{\beta} \rangle$ and we got S' (counting corrected by pressure effect) using Equation (3).

$$\frac{\Delta S'}{S_0} \times 100\% = \frac{\Delta S}{S_0} \times 100\% - \langle \hat{\beta} \rangle \Delta P \quad (3)$$

$S_0 = 161.5 \text{ counts s}^{-1}$ and $P_0 = 963 \text{ hPa}$. This barometric coefficient is consistent with other detector reports (see Maghrabi et al., 2012; Paschalis et al., 2013; Zazyan et al., 2015; Mendonça et al., 2016). Firstly, the barometric coefficient is much higher for the case of neutrons ($\beta \sim -0.7\% \text{ hPa}^{-1}$) than the ionized components. Secondly, for these last ones $\beta \sim -(0.1-0.2)\% \text{ hPa}^{-1}$. Furthermore, the estimated value is consistent with the preliminary values estimated by MITO data, a muon telescope installed near Marambio (Ayuso et al., 2021). This coefficient will depend on the type of particles, their energy and the zenith angle (Mendonça et al., 2019). Thus, the reported value is a global average without distinction between any of the variables mentioned above. In future works, we will analyze the dependence of the barometric coefficient with deposited energy using the charge histograms explained in Section 2.2.

4.2. Temperature Effect

The pressure corrected data show a seasonal modulation with a maximum during August-September (winter-spring) and a minimum during February-March (summer-autumn) with an amplitude of $\sim 3\%$ (see the blue curve on Figure 7 (b)).

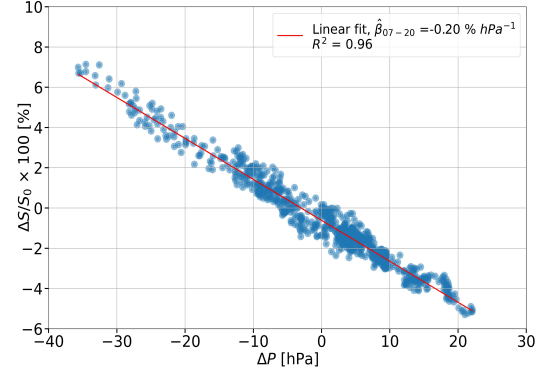


Fig. 4. $\Delta S/S_0 \times 100\%$ vs. ΔP for July 2020. The blue points are the data and the red line is a linear fit.

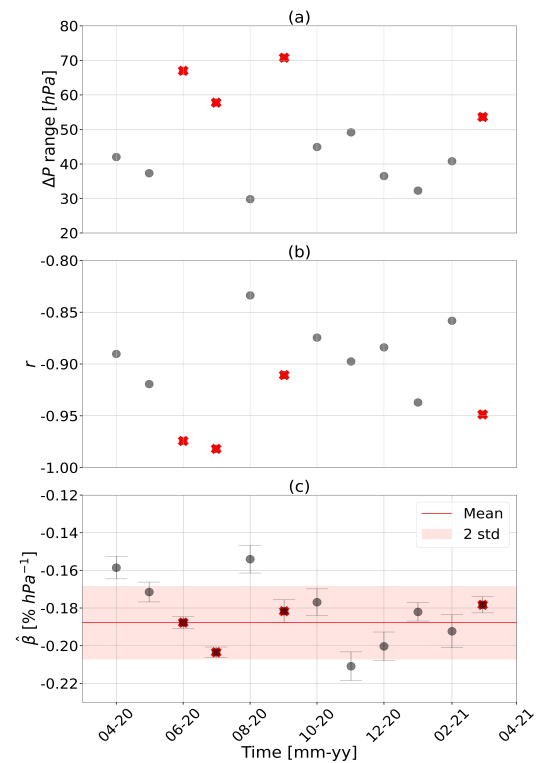


Fig. 5. ΔP range (a), correlation coefficient r (b), and $\hat{\beta}$ as a function of months. The red Xs are months that satisfy the chosen criteria. In (c) the mean beta value and 2 standard deviations are shown.

Particle showers development depends on the primary type, its energy, zenith angle and the atmospheric depth χ vertical profile. This mass distribution is determined by the temperature profile from the observation level to the atmosphere's upper boundary. The most relevant variation in $\chi(h)$ is correlated with the seasonal cycle (heating-expansion and cooling-compression).

We use the ERA5's atmospheric reanalysis to get the geopotential (ϕ) at 37 pressure levels (from 1 hPa to 1000 hPa) at Marambio with a one-hour resolution from April 2020 to March

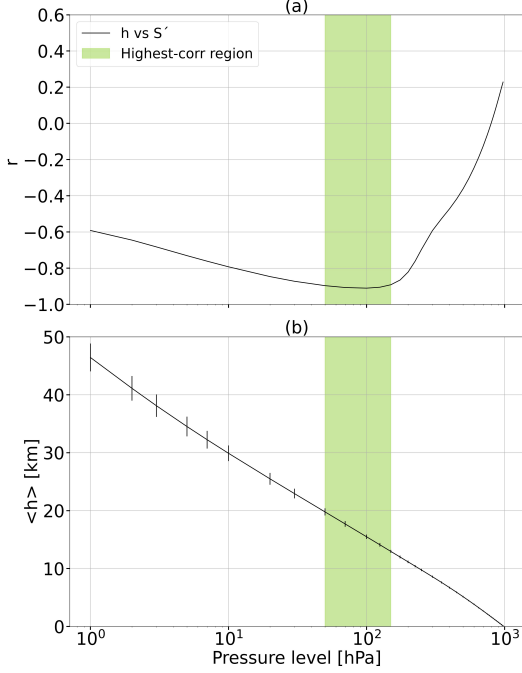


Fig. 6. (a) The correlation coefficient r between the pressure corrected count rate (S') and the altitude for each pressure level. The green area represents the region with the highest correlation. (b) The mean altitude $\langle h \rangle$ associated with each pressure level. The error bars indicate one standard deviation. In both cases the period April 2020-March 2021 is considered.

2021.

ERA5 is the fifth generation model of the European Centre for Medium-Range Weather Forecasts (ECMWF) for atmospheric reanalysis of the global climate. It provides hourly estimates of many environmental variables (Hersbach et al., 2020).

We consider the height h of each pressure level (directly proportional to $\chi(h)$ assuming $g = \text{const}$). In order to get this last one, we consider that geopotential height z can be calculated dividing ϕ by the Earth's mean gravitational acceleration. Then, the height or geometrical altitude is $h = R_e z / (R_e - z)$, where R_e is the Earth's radius. This geometric height is relative to the mean sea level, and it is assumed that the Earth is a perfect sphere.

On Figure 6, (a) the Pearson correlation coefficient (r) for h vs. S' can be seen. The region between 50 and 150 hPa (green area) represents the highest correlation ($r \leq -0.9$). This wide region is expected since contiguous pressure levels are highly correlated with each other. The negative temperature effect is dominating, as it was already said at the beginning of this section (maximum intensity in winter and minimum in summer). On Figure 6 (b), the mean altitude $\langle h \rangle$ for each pressure level is shown. The green region is associated with an altitude of about 13 to 20 km, suggesting that variations in the lower stratosphere region are more determinant than in any other layers.

In this work, we apply the simplest model using only the

height of the level with the highest correlation, which is 100 hPa ($r = -0.91$). Furthermore, this is the level where main muon generation is assumed to take place (Dorman (2004)).

We model the temperature effect on SCRs' counting variability following Equation (4).

$$\begin{aligned} \frac{\Delta S'}{S_0} \times 100\% &= \frac{S'(t) - S_0}{S_0} \times 100\% \\ &= \alpha(H_{100}(t) - H_{100}^0) = \alpha \Delta H_{100} \end{aligned} \quad (4)$$

$\Delta S'/S_0$ is the pressure corrected counting relative variation, α is the atmospheric expansion temperature coefficient given in $\% \text{ km}^{-1}$ and $\Delta H_{100}(t)$ is the altitude variation associated with the isobaric level 100 hPa with respect to its mean value ($H_{100}^0 = 15.5 \text{ km}$). The amplitude of H_{100} 's variation is about 1 km.

In Figure 7 (a), an anti-correlation between $\Delta S'/S_0$ and ΔH_{100} can be observed. The effect of the atmospheric expansion on SCRs' counting was estimated to $\hat{\alpha} = (-3.89 \pm 0.02) \% \text{ km}^{-1}$ (linear temperature coefficient) according to the Equation (4). This coefficient has a value slightly below the reported by the muon telescopes of the GMDN using the same model ($\sim -6\% \text{ km}^{-1}$ in the northern hemisphere and $\sim -5\% \text{ km}^{-1}$ in the southern hemisphere) (Mendonça et al. (2016)). We use $\hat{\alpha}$ to remove the temperature effect considering Equation (5). After that, the variation of the corrected data for pressure and temperature effects (S'') is $<2\%$.

$$\frac{\Delta S''}{S_0} \times 100\% = \frac{\Delta S'}{S_0} \times 100\% - \hat{\alpha} \Delta H_{100} \quad (5)$$

We have chosen a one-year data range to do this analysis in order to remove the seasonal effect. As seen in Figure 7 (b), this model explains not only the seasonal variation, but also shorter-term variations (83% of the total variance).

5. Daily Variation

Assuming that after corrections for pressure and temperature there are not more atmospheric variables affecting the count rate, a spectral analysis will provide periodicities related to heliospheric effects.

There are several techniques to perform a power spectral density (PDS) estimation. Among the nonparametric methods, the Blackman-Tukey method can be found (Blackman & Tukey, 1958). This method is based on the fact that the Fourier transform of an autocorrelation function of a time series is equivalent to its power spectrum. Weighting the autocorrelation function by various shapes is a traditional approach to reduce a power leakage.

We estimate the PSD of the hourly S'' by applying the Blackman-Tukey method and considering the Hanning window of a size equal to 0.3 of the data length. In order to determine the

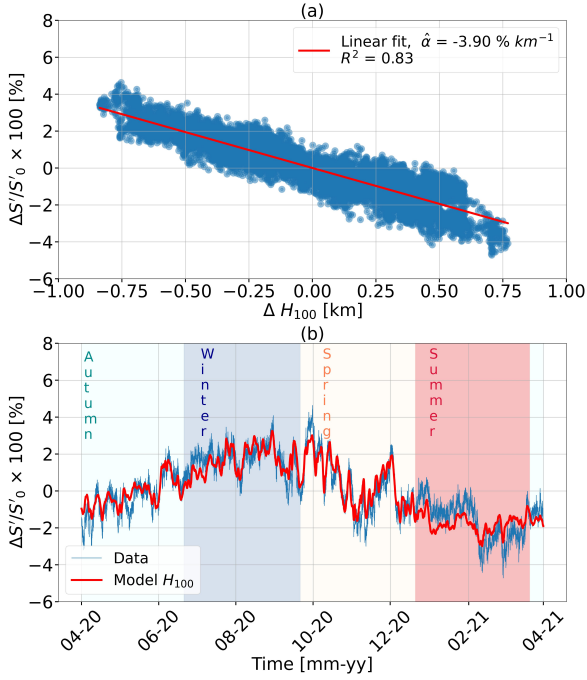


Fig. 7. (a) $\Delta S'/S_0 \times 100$ % vs. ΔH_{100} and (b) $\Delta S'/S_0 \times 100$ % time series for April 2020-March 2021. The blue points are the data and the red line is a linear model based on Equation (4).

spectral peak significance, the generation of a red-noise spectrum has been employed. Spectral peaks which have amplitudes of above the 95 % confidence interval are statistically distinct from the background red-noise spectrum. On Figure 8, the power spectrum is shown in blue. The red line is the red-noise spectrum, and the dashed red line is the 95 % confidence limit. The significant periodicities, indicated by red squares, are: 1, 31.28 and 109.5 days. These periodicities could be associated with the DV, the solar rotation, and the Rieger periodicity, respectively.

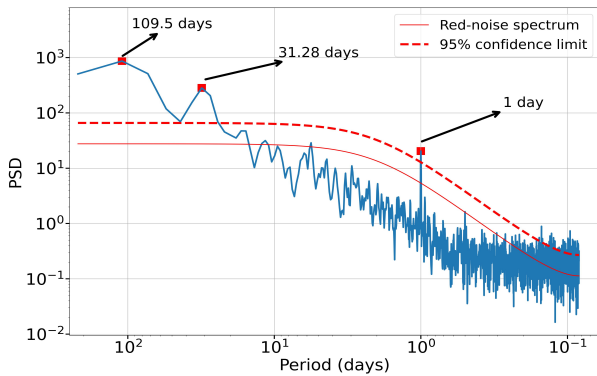


Fig. 8. Power spectrum of the data corrected for pressure and temperature. The red line represents the red-noise spectrum while the dashed red line marks the 95 % confidence limit. Significant periodicities are indicated by red squares.

In this work, we focus on the DV, and we used the superposed epoch analysis (SEA) to obtain the typical profiles of this periodicity. The main aim of the SEA technique is getting an average profile by taking a sample of individual profiles (one-day count rate S'' in this case). Each individual profile has the same number of points or bins in time. The data S'' within each bin are averaged to a single value per bin. In our case, we have $N = 365$ profiles that correspond to 365 days, and each of them has the same bins in time (24 bins of 1 hour long).

In Figure 9 (a) we can see the superposed profile (relative variation) in each season of the year. In all cases, the maximum value is reached between 8 and 12 hr LT and the amplitude is found between 0.08-0.15 %. We expect that, if there is any residual effect of the expansion and compression of the atmosphere during the year, the profile would look different in each season in terms of phase and amplitude. Since this is not observed, our interpretation is that this modulation has a heliospheric and not an atmospheric origin.

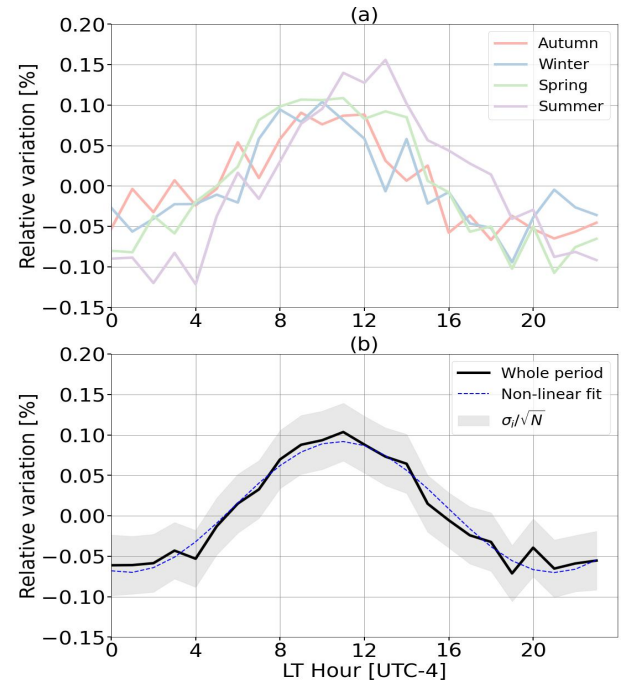


Fig. 9. SEA analysis of the temperature and pressure corrected data (S'') in each season (a) in the whole period (b).

The black curve of Figure 9 (b) shows the superposed profile considering the entire analyzed year (April 2020 - March 2021).

The grey region represents the error of the mean of each hourly bin and the blue line is a non-linear fitting based on Equation (6), assuming a harmonic behaviour as a simplification.

$$A \cos\left(\frac{2\pi}{T}t + \gamma\right) + C \quad (6)$$

$T = 20.2$ hr is the time period, $\gamma = -0.2$ rad is the initial

phase, $C = 0.01\%$ is the mean value of the series, and $A = -0.08\%$ is the amplitude. The maximum is at 11 hr LT.

The DV arises from the spatial anisotropy of the GCR flux reaching Earth due to different physical processes controlling their transport in the interplanetary space. The ground-based detectors record the GCR flux as a rotating lighthouse, pointing their asymptotic cone to a given direction once a day. As shown in Figure 10 (b), the convective-diffusion model assumes two main anisotropies in the ecliptic plane, both point to the direction where the maximum GCR flux comes from: ξ_D a vector parallel/anti-parallel to the IMF and with an outward direction related to the GCRs' diffusion along IMF; ξ_C a vector with an inward radial direction related to the GCRs' outward convection by the solar wind. Assuming that under steady equilibrium conditions there is no net flux of GCRs inward/outward from the Sun, the net spatial anisotropy ξ_{CD} is expected to be found in the 18 hr LT direction as can be seen in Figure 10 (b) (Forman & Gleeson, 1975).

In order to analyze the observed DV of Figure 9 it is necessary to take into account the asymptotic directions of PCRs arriving at Marambio in order to link local time with the spatial IM anisotropy. An observatory located at a longitude LO records SCRs generated by PCRs that entered the magnetosphere at $LO + \delta$, where δ is the longitudinal distance between the mean asymptotic cone and the observatory location (LO). Therefore, the direction of the maximum flux in the interplanetary space is $\tau = LTO + \Delta$, where LTO is the time of the observed maximum expressed in the observatory LT hour and $\Delta = \delta \times 1\text{hr}/15^\circ$ is the time difference between both locations.

Based on Figure 9 (b), the time of the maximum flux at Marambio is $LTO = 11$ hr LT (indicated with an "*" in Figure 10 (b)). Figure 10 (a) shows the asymptotic directions for primary protons projected on the Earth's surface (with rigidities of 3.1, 4.6, 10, 20, 50 and 100 GV) arriving at Marambio ($LO = 56^\circ$) for 15° zenith incidence and eight equispaced incidence azimuth values (figure adapted from Masias-Meza & Dasso (2014)). Considering that the maximum contribution of PCRs in the counting occurs for energy between 10-40 GeV, Marambio's mean position of the asymptotic cone is $\delta \sim +60^\circ$ and $\Delta \sim +4$ hr. Finally, the direction of the observed net anisotropy ξ_{obs} is $\tau = 15$ hr LT in interplanetary space with an amplitude of $\sim 0.08\%$. This amplitude is smaller than the observed by NMs (~ 0.3 - 0.6% , depending on the site's latitude) and similar to MTs. As mentioned in Section 2.2, WCDs are more sensitive to higher primary energies (\sim tens of GeV) than neutron monitors (< 20 GeV). As the solar modulation for primary energies exceeding several tens of GeV is expected to be weaker then, a smaller diurnal amplitude for this type of detector is expected. In order to have more accurate results of the diurnal anisotropy features, the asymptotic cones of viewing have been taken into account in detail as well as the average PCR energy observed.

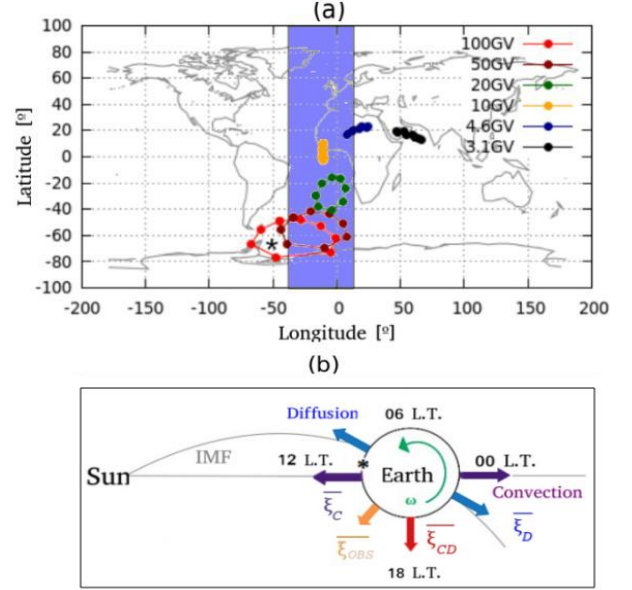


Fig. 10. (a) Asymptotic directions of primary protons before interacting with the geomagnetic field, for different energies and different incidence azimuth angles (MAGCOS numerical simulations) adapted from Masias-Meza & Dasso, 2014. PCRs that contribute the most to the count observed by Neurus enter through the cones found in the violet region. (b) Diagram of the diurnal variation and the different processes involved: the convective anisotropy (ξ_C), diffusive anisotropy (ξ_D), the predicted anisotropy ξ_{CD} by the convective-diffusion theory, and the observed anisotropy ξ_{obs} . The "*" indicates Marambio's location.

6. Summary and Conclusions

We presented a new CR detector based on the water-Cherenkov effect, which is mainly for space weather purposes. It was installed at the Argentine Antarctic base, Marambio, in 2019. This detector is part of the Latin American Giant Observatory (LAGO), an extended cosmic rays observatory operating in Latin America and Antarctica.

This detector has been measuring continuously mainly particles from EM and muonic components of the particle showers since April 2020. It is necessary to have an accurate estimation of the atmospheric modulations from the data to make it suitable for studying solar and interplanetary phenomena and convenient for SW applications so as to observe Forbush decreases and strong ground-level enhancements.

In this work, we describe and correct the atmospheric pressure and temperature effects on the observed SCR flux. We have analyzed observations made during a year (April 2020-March 2021) during which the laboratory room temperature was at an optimal range ($22 - 24^\circ\text{C}$). First, we found the well-known anti-correlation between the count rate and the barometric pressure (measured in the laboratory). We have estimated the barometric coefficient per month by performing linear fits. We got $\langle \hat{\beta} \rangle = (-0.19 \pm 0.02)\% \text{ hPa}^{-1}$ for the whole period. After removing this effect using $\langle \hat{\beta} \rangle$, a clear seasonal effect

is observed as a sinusoidal variation with a maximum during winter, a minimum during summer and an amplitude of $\approx 3\%$.

For the temperature effect, we've worked with data from ERA5's atmospheric reanalysis. We observed that the highest correlation coefficient between pressure corrected data and altitude occurs in the pressure level corresponding to 100 hPa (mean altitude $H_0^{100} = 15.5$ km). The negative temperature effect is dominating. Then we considered the method of effective generation level, which takes into account altitude variations of this pressure level, which is the muon main production layer. We performed a linear fit and got the atmospheric expansion temperature coefficient $\hat{\alpha} = (-3.89 \pm 0.02) \% \text{ km}^{-1}$. This model explained the $\sim 82\%$ of the total variance.

Finally, we performed a spectral analysis to the corrected data for both effects (barometric and temperature) and we observed a significant periodicity of one day. We analyzed this periodicity using SEA and concluded that there are not significant changes in the amplitude or phase during different seasons, thus, this periodicity is due to heliospheric phenomena. For the whole period, we got an amplitude of $\sim 0.08\%$ and the time of the maximum is 15 hr LT in the IM, taking into account the effect of the geomagnetic field, which is consistent with the convection-diffusion theory and previous reports. Thus, we conclude that this detector is able to observe spatial anisotropies of GCR flux as well as other GCRs' properties of interest for Space Weather studies.

7. Acknowledgments

N.A.S. is fellow of CONICET. S.D. and A.M.G are members of the Carrera del Investigador Científico, CONICET.

This work was supported by the Argentinean grants PICT 2019-02754 (FONCyT-ANPCyT) and UBACyT-20020190100247BA (UBA). LAGO collaboration is very grateful to all the participating institutions and The Pierre Auger collaboration for their continuous support.

References

- Arnaldi, L. H., Cazar, D., Audelo, M. et al. (2019). Preliminary results of the design and development of the data acquisition and processing system for the LAGO Collaboration. *PoS, ICRC2019*, 175. doi:10.22323/1.358.0175.
- Asorey, H. (2012). *Los Detectores Cherenkov del Observatorio Pierre Auger y su Aplicación al Estudio de Fondos de Radiación (Water-Cherenkov detectors of the Pierre Auger Observatory and its application to the study of the background radiation)*. Ph.D. thesis Balseiro Institute, Universidad Nacional de Cuyo, Argentina. doi:10.13140/2.1.3041.1846.
- Asorey, H., Núñez, L. A., & Suárez-Durán, M. (2018). Preliminary Results From the Latin American Giant Observatory Space Weather Simulation Chain. *Space Weather*, 16(5), 461–475. doi:10.1002/2017SW001774.
- Ayuso, S., Blanco, J., García Tejedor, J. I. et al. (2021). Mito: a new directional muon telescope. *J. Space Weather. Space Clim.*, 11, 13. doi:10.1051/swsc/2020079.
- Belov, S. M., Zobnin, E., & Yanke, V. G. (2021). Cutoff rigidity and particle trajectories online calculator. *NMDB@Home 2020: Proceedings of the 1st virtual symposium on cosmic ray studies with neutron detectors, 1*, 197–203. doi:10.38072/2748-3150/p24.
- Bertou, X. (2006). Calibration of the surface array of the Pierre Auger Observatory. *Nucl. Instrum. Meth. A*, 568, 839–846. doi:10.1016/j.nima.2006.07.066.
- Bieber, J. W., & Evenson, P. (1995). Spaceship Earth - An Optimized Network of Neutron Monitors. *ICRC1995*, 4, 1316–1319.
- Blackman, R. B., & Tukey, J. W. (1958). The measurement of power spectra from the point of view of communications engineering - part i. *The Bell System Technical Journal*, 37, 185–282. doi:10.1002/j.1538-7305.1958.tb03874.x.
- Blanco, J. J., García-Tejedor, J. I., Óscar García-Población et al. (2022). Cosmic ray observations from livingston island. *Adv. Space. Res.*, 69(9), 3514–3524. doi:10.1016/j.asr.2022.02.046.
- Chilingarian, A., Babayan, V., Karapetyan, T. et al. (2018). The seven worldwide network of particle detectors: 10 years of operation. *Adv. Space. Res.*, 61(10), 2680–2696. doi:10.1016/j.asr.2018.02.030.
- Dasso, S., Asorey, H., & Pierre Auger Collaboration (2012). The scaler mode in the Pierre Auger Observatory to study heliospheric modulation of cosmic rays. *Adv. Space. Res.*, 49(11), 1563–1569. doi:10.1016/j.asr.2011.12.028. arXiv:1204.6196.
- Dasso, S., Gulisano, A. M., Masías-Meza, J. J. et al. (LAGO) (2016). A project to install Water-Cherenkov detectors in the Antarctic Peninsula as part of the LAGO detection network. *PoS, ICRC2015*, 105. doi:10.22323/1.236.0105.
- Dorman, L. (2004). *Cosmic Rays in the Earth's Atmosphere and Underground*. Kluwer Academic, Dordrecht. doi:10.1007/978-1-4020-2113-8.
- Durán, M. S., Asorey, H., Dasso, S. et al. (2016). The LAGO Space Weather program: directional geomagnetic effects, background fluence calculations and multi-spectral data anal. *PoS, ICRC2015*, 142. doi:10.22323/1.236.0142.
- Forman, M. A., & Gleeson, L. J. (1975). Cosmic-ray streaming and anisotropies. *Astrophys. Space Sci.*, 32(1), 77–94. doi:10.1007/BF00646218.
- Gil, A., Kovaltsov, G. A., Mikhailov, V. V. et al. (2018). An Anisotropic Cosmic-Ray Enhancement Event on 07-June-2015: A Possible Origin. *Sol. Phys*, 293(11), 154. doi:10.1007/s11207-018-1375-5.
- Grieder, P. (2001). *Cosmic Rays at Earth*. Elsevier, Amsterdam. doi:10.1016/B978-0-444-50710-5.X5000-3.
- Gulisano, A. M., Dasso, S., Areso, O. et al. (2021). State of the art and challenges of the Argentine space weather laboratory (LAMP) in the Antarctic Peninsula. *Boletín de la Asociación Argentina de Astronomía (Bulletin of the Argentine Astronomy Association)*, 62, 280–285.
- Hersbach, H., Bell, B., Berrisford, P. et al. (2020). The era5 global reanalysis. *Q. J. R. Meteorol. Soc.*, 146(730), 1999–2049. doi:https://doi.org/10.1002/qj.3803.
- Kudela, K., Storini, M., Hofer, M. Y. et al. (2000). Cosmic Rays in Relation to Space Weather. *Space Sci. Rev.*, 93, 153–174. doi:10.1023/A:1026540327564.
- Lanabere, V., Dasso, S., Gulisano, A. M. et al. (2020). Space weather service activities and initiatives at LAMP (Argentinean Space Weather Laboratory group). *Adv. Space. Res.*, 65(9), 2223–2234. doi:10.1016/j.asr.2019.08.016.
- Lanabere, V., Santos, N. A., Dorsch, B. D. et al. (2021). Actividades proto-operativas de meteorología del espacio en Argentina (Proto-operational space weather activities in Argentina). (Space weather service activities in Argentina). *Boletín de la Asociación Argentina de Astronomía (Bulletin of the Argentine Astronomy Association)*, 62, 4–6.
- Maghrabi, A., Al Harbi, H., Al-Mostafa, Z. et al. (2012). The kacst muon detector and its application to cosmic-ray variations studies. *Adv. Space. Res.*, 50(6), 700–711. doi:10.1016/j.asr.2011.10.011.
- Masías-Meza, J., & Dasso, S. (2014). Geomagnetic effects on cosmic ray propagation under different conditions for Buenos Aires and Marambio, Argentina. *Sun geosph.*, 9, 41–47. arXiv:1402.6274.
- Mendonça, R. R. S., Braga, C. R., Echer, E. et al. (2016). The temperature effect in secondary cosmic rays muons observed at the ground: analysis of the global muon detector network data. *Astrophys. J.*, 830(2), 88. doi:10.3847/0004-637x/830/2/88.
- Mendonça, R. R. S., Wang, C., Braga, C. R. et al. (2019). Analysis of cosmic

- rays' atmospheric effects and their relationships to cutoff rigidity and zenith angle using global muon detector network data. *J. Geophys. Res.*, 124(12), 9791–9813. doi:10.1029/2019JA026651.
- Mishev, A., & Usoskin, I. (2020). Current status and possible extension of the global neutron monitor network. *J. Space Weather Space Clim.*, 10, 17. doi:10.1051/swsc/2020020. arXiv:2005.12621.
- Parker, E. (1964). Theory of streaming of cosmic rays and the diurnal variation. *Planet. Space Sci.*, 12(8), 735–749. doi:10.1016/0032-0633(64)90054-6.
- Paschalis, P., Mavromichalaki, H., Yanke, V. et al. (2013). An online application for the barometric coefficient calculation of nmdb stations. *New Astron.*, 19, 10–18. doi:10.1016/j.newast.2012.08.003.
- Pierre Auger Collaboration (1996). The Pierre Auger Project design report. *FERMILAB-PUB-96-024, FERMILAB-DESIGN-1996-02*.
- Pierre Auger Collaboration (2011). The Pierre Auger Observatory scaler mode for the study of solar activity modulation of galactic cosmic rays. *J. Instrum.*, 6(1), 1003. doi:10.1088/1748-0221/6/01/P01003.
- Pierre Auger Collaboration (2015). The pierre auger cosmic ray observatory. *Nucl. Instrum. Methods. Phys. Res. A*, 798, 172–213. doi:https://doi.org/10.1016/j.nima.2015.06.058.
- Potgieter, M. (2013). Solar modulation of cosmic rays. *Living Rev. Sol. Phys.*, 10. doi:10.12942/lrsp-2013-3.
- Rockenbach, M., Dal Lago, A., Schuch, N. J. et al. (2014). Global muon detector network used for Space Weather applications. *Space. Sci. Rev.*, 182, 1–18. doi:10.1007/s11214-014-0048-4.
- Sabbah, I. (2013). Solar magnetic polarity dependency of the cosmic ray diurnal variation. *J. Geophys. Res.*, 118(8), 4739–4747. doi:10.1002/jgra.50431.
- Sarmiento-Cano, C., Suárez-Durán, M., Calderón-Ardila, R. et al. (2022). The arti framework: Cosmic rays atmospheric background simulations. *Eur. Phys. J. C*, accepted. doi:https://doi.org/10.48550/arXiv.2010.14591.
- Sarmiento-Cano, C., Suárez-Durán, M., Vásquez Ramírez, A. et al. (2019). Modeling the LAGO's detectors response to secondary particles at ground level from the Antarctic to Mexico. *PoS, ICRC2019*, 412. doi:10.22323/1.358.0412.
- Sidelnik, I. (LAGO) (2016). The Sites of the Latin American Giant Observatory. *PoS, ICRC2015*, 665. doi:10.22323/1.236.0665.
- Sidelnik, I., & Asorey, H. (2017). LAGO: The Latin American giant observatory. *Nucl. Instrum. Methods. Phys. Res. A*, 876, 173–175. doi:10.1016/j.nima.2017.02.069.
- Sidelnik, I., Asorey, H., Guarín, N. et al. (2020). Simulation of 500 MeV neutrons by using NaCl doped Water Cherenkov detector. *Advances in Space Research*, 65(9), 2216–2222. doi:10.1016/j.asr.2020.02.024.
- Simpson, J. A. (2000). The Cosmic Ray Nucleonic Component: The invention and scientific uses of the neutron monitor - (Keynote Lecture). *Space Sci. Rev.*, 93, 11–32. doi:10.1023/A:1026567706183.
- Tezari, A., Mavromichalaki, H., Katsinis, D. et al. (2016). Latitudinal and longitudinal dependence of the cosmic ray diurnal anisotropy during 2001–2014. *Ann. Geophys.*, 34(11), 1053–1068. doi:10.5194/angeo-34-1053-2016.
- Tilav, S., Desiati, P., Kuwabara, T. et al. (2010). Atmospheric variations as observed by IceCube. *ICRC2009*, 1, 10–14. URL: https://ui.adsabs.harvard.edu/abs/2010arXiv1001.0776T.
- Zanini, A., Ciancio, V., Laurenza, M. et al. (2017). Environmental radiation dosimetry at argentine antarctic marambio base: preliminary results. *J. Environ. Radioact.*, 175-176, 149–157. doi:10.1016/j.jenvrad.2017.04.011.
- Zazyan, M., Ganeva, M., Berkova, M. et al. (2015). Atmospheric effect corrections of MuSTAnG data. *J. Space Weather. Space Clim.*, 5, A6. doi:10.1051/swsc/2015007.